Sliding mode control applied to a square-back Ahmed body

Camila Chovet, Maxime Feingesicht, Baptiste Plumejeau, Marc Lippert, Laurent Keirsbulck, Franck Kerhervé, Andrey Polyakov, Jean-Pierre Richard, Wafik Abassi, Jean-Marc Foucaut

Sliding mode control applied to a square-back Ahmed body

Camila Chovet[a,*], Maxime Feingesicht[1], Baptiste Plumjeau[a,e], Marc Lippert[a], Laurent Keirsbulck[a], Franck Kerhervé[c], Andrey Polyakov[e], Jean-Pierre Richard[d], Wafik Abassi[c], Jean-Marc Foucaut[f]

[a]Lamih Umr *8201, F-59313, Valenciennes, France*
[b]*Inria/CRIStAL* Umr9189, *59651 Villeneuve-d'Ascq, France*
[c]*Institut P'* Upr3346, *86962 Poitiers, France*
[d]Ipsa,*94200 Paris, France*
[e]Central Lille, *59651 Villeneuve-d'Ascq, France*
[f]Lml Umr8107, *59650 Villeneuve d'Ascq, France*

Abstract

We consider the first closed-loop separation control experiment on an Ahmed body using a robust, model-based strategy called "sliding mode control" (SMC). The goal is to reduce and further maintain the aerodynamic drag of the square-back Ahmed body flow at $Re_h = 9 \times 10^4$ (based on the body height). This study also investigates the practical feasibility of this approach which shows a great promise for industrial applications. The flow is manipulated by a slotted jet placed on the top trailing edge, combined with a predefined angle direction, and sensed by a drag balance. Base pressure and lift measurements are also obtained in real-time. The interaction between the air jet actuator and the mean near-wake flow are depicted by means of Particle Image Velocimetry. In order to compare this closed-loop strategy we first present two open-loop ones. Continuous blowing is initially used to directly influence the recirculation area and hence achieve a reduction in the drag. Approximately a drag reduction of 8% is accomplished making this approach the "optimal case" control strategy. However, because steady blowing mechanisms lead to the highest energy consumption scheme, this strategy will only serve as the first open-loop control reference. The second open-loop strategy involves three periodic forcing frequencies, St_A = 0.0765, 0.135 & 0.405. The influence of these frequencies on the near-wake, and its further drag modification, will be further examined. The proposed sliding mode control (closed-loop strategy) is applied to the same Ahmed body configuration and compared to the open-loop cases. It will be designed on the basis of a simplified input-output model which was recently defined for another flow control application. Last, a second experiment is conducted so to show the disturbance rejection of the controller, corroborating the robustness and efficiency of this control approach. Its limitations and difficulties on an experimental setup are also discussed. SMC is able to reduce and maintain the drag to a desire set-point regardless external flow perturbations. Our control strategy was recently used in another context (flow reattachement on a wing) with the same robustness. These successes make guess it is applicable to multiple experimental and industrial contexts.

Keywords: sliding mode control, bilinear time-delay model, flow control, drag reduction unsteadiness of separated flows

*Corresponding author (Camila Chovet)
Email address: camila.chovet@univ-valenciennes.fr

1. Introduction

The flow around a vehicle is inherently three-dimensional and presents highly complex characteristics. The effects of these flows on the vehicle's aerodynamic performance is strongly related to fuel consumption and greenhouse gas emission [37]. Therefore, a thorough investigation to understand and control these flows has been done over the years [34, 6, 50, 38, 39, 8]. Most previous studies have investigated the aerodynamics of heavy vehicles relying on mean flow characteristics, but the unsteady flow phenomena are much more related to the mechanism of aerodynamic force generation and its control [17] . A bluff-body model induces large recirculation bubbles with low-pressure wake. The recirculating flow itself is absolutely unstable and produces self-sustained large-scale flow oscillations [35]. The massive separation at the edge of the body and pressure drop at the base are the main contributors to aerodynamic drag, the latter representing over 65% of the total power expense [42] at highway speeds. If a 20% aerodynamic drag reduction is achieved at 105 km/h for a tractor-trailer weighing 36 tons, 4% of the fuel could be saved [12]. The manipulation and/or control of the wake flow provides a great potential to achieve drag reduction. This approach is therefore of great challenge for transport industry which may be tackle as a multidisciplinary field.

Flow control can be divided into three groups: passive, active open-loop and active closed-loop. Various passive means for bluff-body flow control are well-investigated and have been applied in numerous experiments [55, 44]. The most effective ones for drag reduction were found to be base cavities and boat tails [17]. The first one consists of four extensions from the edge of the base forming a cavity, the second one is a tapering extension with a slant angle. However, passive devices may have an adverse effect away from the specific operating conditions for which they were designed. An alternative relates with active flow control (AFC). Such devices can reproduce effects of passive ones but can, in addition, adapt to changing flow conditions while being operating in open-loop or closed-loop manner. Moreover, a combination of passive and active devices might gain additional base pressure recovery by enhancing the shear layer deflection [21, 53]. An extensive overview of possible actuators for AFC is given in Cattafesta & Shelpak [15]. The benefit of active devices for car manufacturers is however still to be demonstrated.

The most common open-loop strategies for buff-body are, steady blowing/suction of air flow [5] or unsteady synthetic/pulsed jets on the separation trailing edges [30, 45, 14]. The majority of these studies are dedicated to manipulate the wake by forcing the separated shear layer. Low-frequency forcing, which targets intrinsic flow instability, was extensively considered and was found to amplify the development of the shear-layer. In contrast, high-frequency forcing has been demonstrated to result in an enhancement of energy transfer from large to small scales and a substantial increase in the dissipation and in the decay rate of turbulent kinetic energy [59], resulting in lower entrainment and increase of the bubble size or of the base pressure. Pastoor *et al.* [48] achieved a significant drag reduction and a suppression of vortex shedding in the wake by open-loop forcing, both in experiment and LES. Rouméas *et al.* [52] simulated an open-loop active flow control using steady blowing devices at the edges of the back of the body, with a total drag reduction of up to 29%. Barros *et al.* [7] exemplified the capabilities of both increasing or decreasing the turbulent fluctuations across a canonical mixing layer by applying low- or high-frequency forcing, respectively.

Open-loop flow control is pre-determined and is somewhat independent of the flow state, incapable to adapt to changing flow conditions. In contrast, closed-loop control offers potential to increase robustness and efficiency of the control device and constitutes an active research area [48, 27, 41]. Based on design efforts for an "in-time" time scale, closed-loop control can be divided in two categories [37], namely, (i) model-free and (ii) model-based approaches.

In a model-free form, no underlying model is required. In-time model-free control may be performed, for example, by a simple proportional-integral-derivative (PID) controller [61]. While widely used in many industrial processes, there ex-

ist no generic simple recipes for tuning the parameters of such controller particulary when the control system has uncertainties such as for example modeling errors. Unsupervised generic methodology based on machine learning which can exploit arbitrary nonlinearities in complex systems has recently gain traction on the past years in the fluid mechanics community to, literarily, learn a control law. As a pioneer work, Noack and co-authors used genetic programming to achieve both structure and parameters identification of control laws in the context of various turbulence flow control problems even at high Reynolds numbers [46, 29, 20, 18]. One of the obstacles of using machine learning, such as introduced in Duriez *et al.* [20], is that a large number of experiments are required to fulfill the criterion of statistical convergence.

Alternatively, a well established framework for the stabilization of flows with model-based control already exists. When derived directly from the Navier-Stokes equations these models are of very high order and require reduction before they can be used in a realistic setting [28]. Furthermore, turbulent flow is characterized by broadband frequency dynamics with complex frequency cross-talk, where the mathematical modeling of the non-linearities constitutes a great challenge. A large portion of the turbulent flow controllers are derived from a reduced-order model, using previous knowledge of the physics of the flow. The physical analysis of the flow can yield simple models leading to efficient control laws [48, 16]. The second option is system identification using experimentally obtained black-box models (seeks to build an input-output model of the flow from empirical observations). The flow is probed until a model can be derived from its responses. This approach has been successfully applied to turbulent separated flows configurations [10, 41].

Following the latter perspective, we employ a robust model-based strategy (previously used in another context -flow reattachement on a wing- [25]) to control, reduce and maintain in a desired value the aerodynamic drag of a square-back Ahmed body. This approach is refereed as sliding mode control (SMC). The feasibility and robustness of this approach in an perturbed experimental setting is questioned. Pulsed actuators were installed at the trailing edge of the model. We experimentally study the effect of open- and closed-loop flow control on the coherent structures in the near-wake. For the open-loop control case, steady blowing and periodic forcing approaches are analysed. To educe the physical mechanisms involved in this flow, static pressure, drag and lift forces, and time-resolved Particle Image Velocimetry synchronized measurements were performed. The paper is organized as follows. In §2, we describe the set-up apparatus of the generic car model. The sensor-based control strategy based on sliding mode control is proposed in §3. Open- and closed-loop results are detailed in §4. Finally, we summarize the main findings and provide future industrial and research directions in §5.

2. Experimental apparatus

In this section, we describe the experimental facility including the wind tunnel, actuation system, pressure, force and velocity measurements. The details of the real-time system used for the flow control are also presented.

2.1. Flow configuration

Experiments were conducted in a closed-loop wind tunnel. Its test section is 2m wide, 2m high and 10m long. The maximum free-stream velocity is about 60m/s with a turbulence intensity of approximately 0.6%. The blunt-edged bluff body is a simplified car model similar to a square back Ahmed body [1]. The model has the following dimensions: height h=0.135m, width w=0.170m and length l=0.370m (Figure 1 (a)). Its front edges are rounded with a radius r=0.05m. The model was mounted over a raised floor with a sharp leading-edge to control the boundary layer thickness (with the following dimensions front length $l_a : 0.315m$, back length $l_b : 0.315m$, width $W : 0.4m$). The back length l_b is large enough to have a complete wake development. The model was installed with a ground clearance of g=0.035m (Figure 1 (b)). A support fixed the geometry to the ground and connect it to a drag balance, the blockage ratio was 0.57%. The flow was described in a Cartesian coordinate system with x, y and z representing

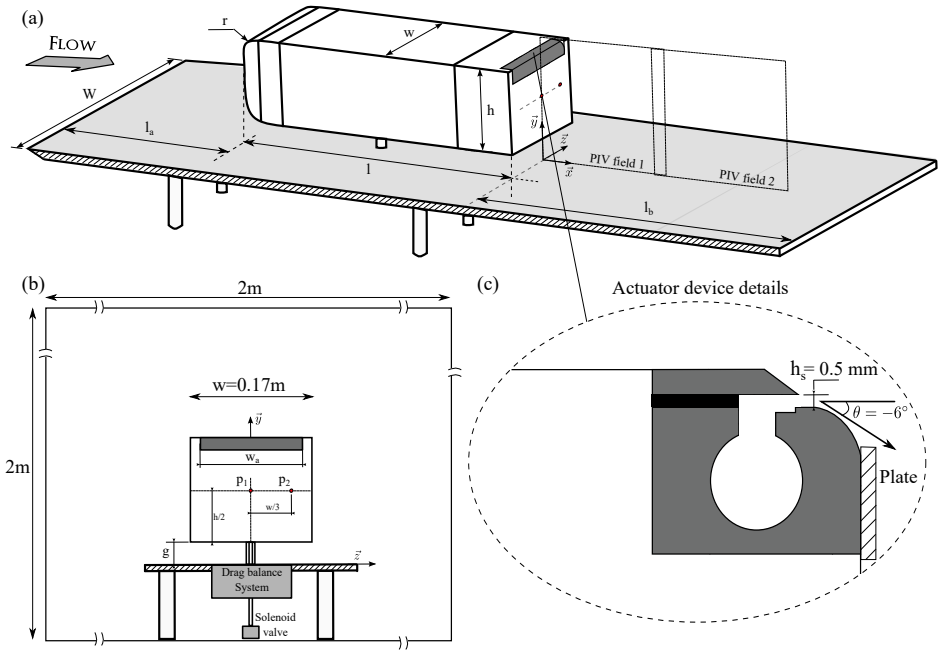

Figure 1: Setup

streamwise, transverse (normal to ground) and spanwise directions, respectively. The origin was placed on the raised floor at the streamwise position of the rear surface. All the results in this paper were obtained with a constant free-stream velocity U_∞ = 10 m/s, with a corresponding Reynolds number based on the model height of $Re_h = 9 \times 10^4$.

2.2. Measurements setup

2.2.1. Time resolved measurements

Two sub-miniature piezo-resistive Kulite XCQ-062 sensors, being able to measure the unsteady pressure with a nominal measurement range of 35kPa, were placed at the back of the Ahmed body. These sensors were placed just to have a local view of the base pressure, they will not be used for closed-loop control. The first flush-mounted Kulite transducers, p_1 was located at the center plane at $h/2$ from the bottom of the body and p_2 was at a spanwise distance of the mid-span of $z = w/3$ (Fig. 1 (b)). The jet velocity was measured using a hot-wire Dantec anemometer at the jet exit plane, the wire (55P15) was positioned parallel to the slot. The sample frequency was 10kHz with a cutoff frequency of 3kHz. The velocity data were phase averaged over a full period (T) in order to determine the mean velocity of the jet V_j. Drag force was measured using a 6-components DELTA ATI aerodynamic balance model built in the raised floor. The balance has a sensing range, for the drag and lift, of 0 to 165N, with a resolution of 0.03N and a high signal-to-noise ratio. The maximum error associated with repeatability and hysteresis was found to be approximately 0.5%.

2.2.2. PIV *parameters and procedure*

The velocity flow fields were obtained using a standard two-component TSI particle image velocimetry (PIV) system. The flow is seeded with oil particles using a jet atomizer upstream of the stagnation chamber. This location allows homogenous dispersion of the particles throughout the test section. The system consists of a double-pulse laser system generating the light sheet and two cameras (2000×2000 pixels charge-coupled-device Powerview

Cases	$C_\mu(\%)$	St_A	L_r/h
Natural flow (ref)		-	1.15
Steady blowing	1.355	0	0.87
		0.0675	0.83
Forcing frequency	0.678	0.1350	0.85
		0.4050	0.84

Table 1: PIV cases and associated parameters.

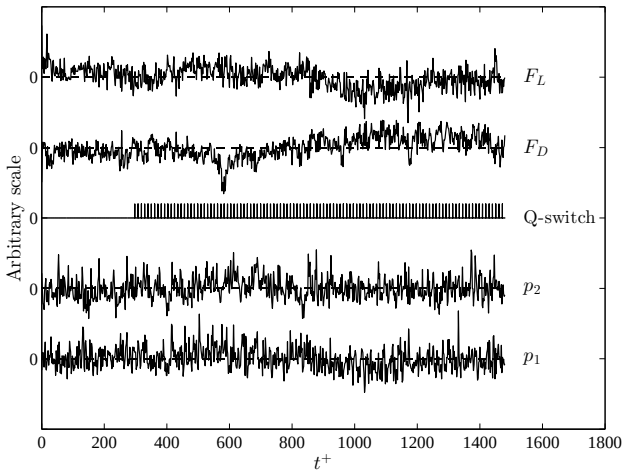

Figure 2: Example of simultaneous measurement of the Q-switch signal of the laser cavity B and the unsteady pressures (p_1 and p_2) and forces (F_D and F_L) during a PIV acquisition. + subscript denotes the h/U_∞ normalisation.

with a 50mm optical lens) recording the light scattered by the tracer particles. The frequency-doubled laser (Q-switched Nd:YAG operating at 532nm; dual-head BigSky) emits laser pulses with a maximum energy of 200mJ. A multipass algorithm with a final interrogation window size of 16×16 pixels^2 and 50% overlapping is applied. The resulting PIV domain is about 3.7h×1.8h on the x-y plane passing through the middle plane of the Ahmed body as shown in Figure 1 (a). For every test case (reported in Table 1), 2000 double-frame pictures were registered to assure velocity fields statistics convergence. The PIV time-uncorrelated snapshots were recorded with a repetition rate of a 7Hz. In order to maintain the causality between the dynamical aspect (instantaneous flow fields) and the global behaviour (drag, lift and surface-pressures time-histories) of the bluff body, the unsteady pressure measurements had to be acquire simultaneously with the PIV. To achieve synchronization, the Q-switch signal of the laser cavity B was recorded simultaneously with the pressure transducer and forces signals using a 32-channel A/D converter Dewesoft data acquisition system, with a sampling frequency of 20kHz. A cutoff filtered at 6kHz for the Q-switch and a second one at 1kHz with a cutoff filtered of 300Hz were used. An example of the synchronization is shown in Figure 2.

2.3. Actuation device

The model is equipped with an actuator slit at the top trailing edge, as illustrated in Figure 1(c). The slit width is $h_s = 0.5mm$ and the actuation length is $w_a = 150\ mm$. Due to a narrow slit width the jet velocity can go up to 55 m/s. The pressured air, supplied by a compressed air reservoir, can be blown tangentially to the free-stream velocity through the slit (Figure 3). The pulsed blowing is driven by a FESTO-MH2 solenoid valve that can generate an on/off pulsed jet within an actuation frequency range between $f_A = 0 - 500Hz$. The solenoid valve was placed under the raised floor. A rounded surface, adjacent to the slit exit, with an additional plate is installed to blow the jet in a predefined direction (for this case we used an actuation an $\theta = -6°$. Figure 3 shows a close-up view of the surface at the exit zone. This surface resembles a boat tail (Coanda effect) passive device for drag reduction. It is well known that the length and slant angle of the boat tail can strongly affect the drag-reduction performance [33, 60]. Figure 4 shows the jet velocity variation during an operation cycle for an actuation frequency of 1Hz. When the actuator is activated ($t/T = 0$), a settling time is observed due to the travelling distance between the solenoid valve and the actuator. When the control is turned off, again a brief time-delay is also observed. This time-delay can be critical for higher actuation frequencies and can strongly affect the jet flow behavior as shown in Figure 4 by

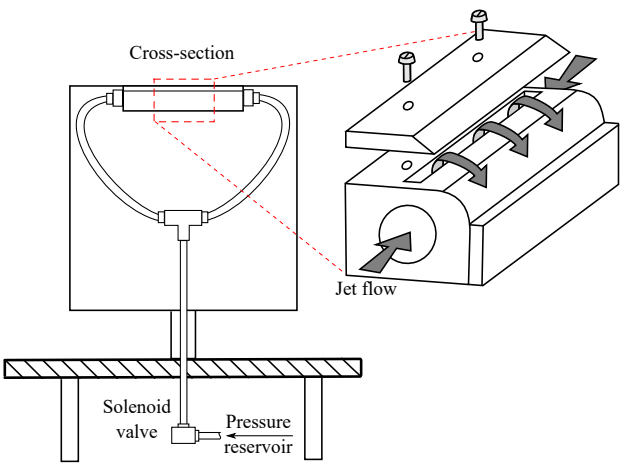

Figure 3: Front view of actuation system. Closed-up view of the actuator mechanism.

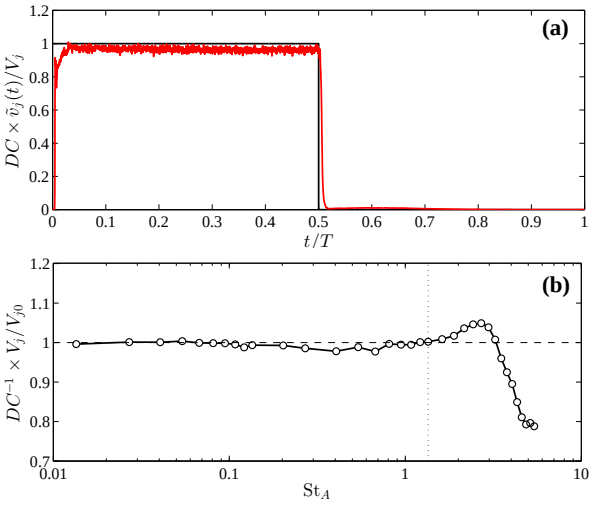

Figure 4: **(a)** — Normalized phase average of the jet velocity $v_j(t)$ measured at 1mm downstream the centerline of the slit exit by use of a single hot-wire probe. — Solenoid valve control. **(b)** Frequency response of the actuation device. The phase average operator is denote by the superscript $\tilde{}$. V_j is the mean velocity of the jet, V_{j0} is the mean velocity of the jet in steady blowing and DC is the duty cycle.

the frequency response of the actuation device. The mean velocity jet exhibits constant values until a pulsating frequency of 100Hz ($St_A = f_A.h/U_\infty = 1.35$). After this critical value, the mean velocity of the jet strongly depends on the actuation frequency. A variation of the mean jet velocity V_j is caused by a modification on the actuation frequency f_A, duty cycle DC and/or supply pressure P_a. Consequently, in order to keep a constant injection velocity, a maximum actuation frequency of 100Hz will be used. We choose a pressure value of $P_a = 6bars$ and a forcing frequency control DC of 50%, giving a maximum jet velocity of 32.2m/s. The mean jet velocity V_j is equal to 16.1m/s for periodic forcing, while in steady blowing configuration the velocity V_{j0} will reach its maximum value 32.2m/s. The jet velocity was quantified, as defined by Amitay *et al.* [3], by the momentum coefficient:

$$C_\mu = \frac{S_j V_j^2}{(1/2) S U_\infty^2} = DC \times C_{\mu 0}$$

Where S and S_j are respectively the slit and the Ahmed cross-sectional area and V_j the mean jet velocity. $C_{\mu 0}$ refers to the steady blowing momentum coefficient.

2.4. Real-time system

The real-time processing was achieved using an Arduino board [4]. An Arduino Uno is sufficient for the control developped here but an Arduino Mega could be used if more memory is needed to store data from more sensors. The data is measured from the sensors using the analogue inputs of the Arduino and the measurements are sent to a computer using the serial connection of the Arduino, connected to a USB port of the computer. The control is sent to the actuators using a digital output port of the Arduino. The sampling rate was fixed at 100Hz. Higher sampling rates can be achieved by sending less text or data through the serial connection. In this case, every measured data was sent even if it was not used in the control algorithm (i.e. the drift) and the text chain sent contains a significant amount of unnecessary text in order to make it easily readable when received on the computer. The sampling rate of 100Hz was experimentally proven to be sufficient for the control algorithm developped in this paper while being attainable by the Arduino.

3. Sliding mode feedback control

In this section, we present a novel, robust closed-loop approach to reduce the drag of the Ahmed body. We explore the opportunities of sensor-based control using an approach referred as sliding mode control (SMC). The principle of the sliding mode control will be thoroughly explained in (§3.1). In (§3.2), an initial SISO black-box model identification is presented using the bilinear model approach presented by Feingesicht *et al.* [25].

3.1. SMC *Principle*

The problem of a set-point tracking is considered for a control system of the form,

$$\dot{s}(t) = f(s,t) + g(s,t)b(t) \tag{1}$$

where f and g are uncertain functions and $b(t) \in \{0,1\}$ is the relay control input. The objective is to determine a control that guarantees $s(t) \to s^*$ as $t \to +\infty$, where s^* is a desired set-point. The control must be also robust with respect to some uncertainties in f and g. A convenient set-point tracking as well as precise disturbance rejection are desirable qualities. If we can respect the dynamics of the system to lie on a well behaved surface, then the control problem is greatly simplified. Sliding mode control SMC [56] is based on the design of an adequate "sliding surface" (or "sliding manifold") defined as,

$$\Sigma = \{(s,t) \mid \sigma(s,t) = 0\} \tag{2}$$

that divides the state space into two parts which correspond to one of the two controls which commutate from one to zero when the state crosses the surface in order to maintain the sliding mode $\sigma(s(t),t) = 0$. The manifold Σ is defined in such a way that the error $|s(t) - s^*|$ vanishes to zero when the system state $s(t)$ is restricted to lie on this surface. The control problem then reduces the problem of reaching phase during which trajectories starting off the manifold Σ move toward it in a finite time, followed by a sliding phase during which the motion is confined to the manifold and the dynamics of the system are represented by the reduced-order model.

3.1.1. Introducing example

The sliding mode control principle can be illustrated using a simple example. Let consider the following system,

$$\dot{s}(t) = -\alpha s(t) + \beta b(t) \tag{3}$$

with $\alpha > 0$, $\beta > 0$, $s(0) \in [0, s_{\max})$, $s_{max} = \beta/\alpha$ and $b(t) \in \{0,1\}$, that has a bounded positive solution $0 \le s(t) < s_{max}$ for any input signal b, since,

$$s(t) = e^{-\alpha t}s(0) + \beta \int_0^t e^{-\alpha(t-\tau)}b(\tau)d\tau < s_{\max}. \tag{4}$$

Let us consider the simple sliding variable $\sigma(t) = s(t) - s^*$, which can be treated as a measure of how far the state $s(t)$ from the desired set-point s^* is. The main idea is monitoring the sign of $\sigma(t)$ in order to decide when it is necessary to switch the control. Let $s^* \in (0, s_{\max})$ and

$$b(t) = \begin{cases} 1 & \text{if} \quad \sigma(t) < 0, \\ 0 & \text{if} \quad \sigma(t) > 0. \end{cases} \tag{5}$$

In this case, the time derivative of the sliding variable is $\dot{\sigma}(t) = \dot{s}(t) = -\alpha s(t) + \beta b(t)$ and one has

$$\dot{\sigma}(t) = -\alpha s(t) + \beta > -\alpha s^* + \beta > 0 \quad \text{if} \quad \sigma(t) < 0 \tag{6}$$

and

$$\dot{\sigma}(t) = -\alpha s(t) < -\alpha s^* < 0 \quad \text{if} \quad \sigma(t) > 0. \tag{7}$$

Therefore, $\dot{\sigma}(t)\sigma(t) < 0$ for $t > 0$ and $\sigma(t) \to 0$ as $t \to +\infty$. Moreover, according to Utkin [56] the sliding mode on the surface $\sigma = 0$ arises in a finite time, i.e. there exists $t^* > 0$ such that $\sigma(t) = s(t) - s^* = 0$ for $t > t^*$ (see Figure 5).

3.1.2. SMC *with input delay*

The conventional sliding mode control methodology is originally developed for delay-free systems. Simulation (see blue line on Figure 5) shows the resulting oscillations due to the input delay. This simple example points out the behavior changes arising in relay-delay systems, and motivates the study of specific SMC design for systems with state and/or input delay [51]. In order to design the sliding mode

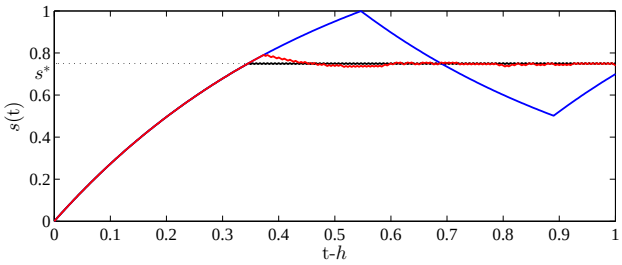

Figure 5: Numerical simulation of the dynamical system for $\alpha = 2$, $\beta = 3$ and for the set-point $s^* = -\beta/(2\alpha)$ with a maximum switching frequency f_{sw} of 300 Hz. Black line: $s(t)$ without input delay, blue line: $s(t)$ with input delay $h = 60/f_{sw}$ and without delay compensation, and red line: $s(t)$ with input delay $h = 60/f_{sw}$ and with the delay compensation.

control, we need to use some technique for compensation of input delay, see e.g. Polyakov [49], Feingesicht *et al.* [25] and references therein. Suppose that the system considered above has input delay:

$$\dot{s}(t) = -\alpha s(t) + \beta b(t-h) \tag{8}$$

where $\alpha > 0$, $\beta > 0$, $h > 0$ and $b(t) \in \{0,1\}$. As the previous one, this system have a bounded positive solutions $0 < s(t) < s_{max}$ with $s_{max} = -\beta/\alpha$ for any input signal b and any $s(0) \in [0, s_{\max}]$. Let us consider the following sliding variable:

$$\sigma(t) = s(t) + \beta \int_{t-h}^{t} b(\tau)\mathrm{d}\tau - \sigma^* \tag{9}$$

where $\sigma^* = s^*(1+\alpha h) > 0$ and

$$s^* \in \left(\frac{\beta h}{1+\alpha h}, \frac{s_{\max}}{1+\alpha h}\right) \tag{10}$$

are selected such that the identity $\sigma(t) = 0$ for $t > t^*$ implies $s(t) \to s^*$ as $t \to +\infty$. Indeed, since $\dot{\sigma}(t) = -\alpha s(t) + \beta b(t)$ then the control input b in the latter equation is not delayed with respect to the sliding variable σ, so the conventional sliding mode design scheme can be utilized [56]:

$$\dot{\sigma}(t) = -\alpha s(t) + \beta > -\alpha\sigma^* + \beta > 0 \;\text{ if }\; \sigma(t) < 0 \tag{11}$$

and

$$\dot{\sigma}(t) = -\alpha s(t) < -\alpha(\sigma^* - \beta h) < 0 \;\text{ if }\; \sigma(t) > 0. \tag{12}$$

Similarly to the previous example we conclude that there exists $t^* > 0$ such that $\sigma(t) = 0$ for $t > t^*$ and using equivalent control method we derive $\dot{\sigma}(t) = -\alpha s(t) + \beta b_{eq}(t) = 0$ with $b_{eq}(t) \in (0,1)$ and

$$\sigma(t) = s(t) + \alpha \int_{t-h}^{t} s(\tau)\mathrm{d}\tau - s^*(1+\alpha h) = 0 \quad \text{for} \quad t > t^*. \tag{13}$$

It can be shown that the latter identity implies that $s(t) \to s^*$ as $t \to +\infty$.
The simulation of the delayed dynamical system taking into account the input delay is shown in Figure 5. Using the presented scheme of sliding surface design, the set-point is reached asymptotically and the oscillations observed previously for input delay system disappear.

3.1.3. Robustness with respect to perturbations

Any mathematical model is just an approximation of reality. The parameters of the model can be found from experimental data with, generally, some errors (due to measurements noise, quantization of digital signals, etc). Therefore, the robustness is the very important issue in the design of model-based controllers. This paper studies robustness of the control system in the sense of input-to-state stability (see Sontag *et al.* [54] for mode details). In our case, this means that the tracking error of robust control system must be proportional to a continuous function of disturbance magnitude.

Let the control system be perturbed as follows,

$$\dot{s}(t) = -\alpha s(t) + \beta b(t-h) + p(t), \tag{14}$$

where s, α, β are as before, $h \in (0,1)$ and $p(t)$ is a perturbation that does not degrade positivity of the system, i.e. $p(t) \geq 0$ if $s(t) = 0$. Let us assume also that the function p is bounded,

$$|p(t)| \leq p_{\max} < \frac{\alpha\beta(1-h)}{1+\alpha} \quad \text{for} \quad t \geq 0. \tag{15}$$

Note that $p(t)$ may contain parametric uncertainty of the system, i.e. $\dot{s}(t) = -(\alpha + \Delta\alpha)s(t) + (\beta + \Delta\beta)b(t-h) = -\alpha s(t) + \beta u(t-h) + p(t)$, where $p(t) = -\Delta\alpha s(t) + \Delta b(t-h)$ and $\Delta\alpha$, $\Delta\beta$ describe errors of

parameters identification. Repeating the above considerations for

$$s^* \in \left(\frac{\beta h + p_{\max}/\alpha}{1+\alpha h}, \frac{\beta - p_{\max}}{1+\alpha h} \right) \tag{16}$$

one can derive $\dot{\sigma}(t) = -\alpha s(t) + \beta b(t) + p(t)$ leading to,

$$\dot{\sigma}(t) > -\alpha\sigma^* + \beta - p_{\max} > 0 \;\text{ if }\; \sigma(t) < 0 \tag{17}$$

and

$$\dot{\sigma}(t) < -\alpha(\sigma^* - \beta h) + p_{\max} < 0 \;\text{ if }\; \sigma(t) > 0. \tag{18}$$

In other words, we again derive $\sigma(t) = 0$ for $t > t^*$ and

$$s(t) + \alpha \int_{t-h}^{t} s(\tau)\mathrm{d}\tau - s^*(1+\alpha h) = \int_{t-h}^{t} p(\tau)\mathrm{d}\tau \;\text{ for }\; t > t^*. \tag{19}$$

Since p is bounded by $p_{\max}$ then the latter identity implies $\|s(t) - s^*\| = O(p_{\max} h)$ for sufficiently large $t > t^*$. This proves the robustness of the proposed SMC.

3.2. SMC *for flow control system*

An identification procedure of the dynamical system is employed here for flow control application. In the present case, the sensor output utilized is the instantaneous drag $F_D(t)$, the control variable $s(t) = F_D^\infty - F_D(t)$, where F_D^∞ is a drag in the uncontrolled steady state, and the control command is the switching function $b(t)$ send to the actuators.

3.2.1. System identification

A black-box SISO modelling approach is considered. Due to the non-linear nature of the governing equations driven the flow dynamics, non-linear models with time-delays are here preferred. The bilinear model proposed by Feingesicht *et al.* [24, 25] is here considered and can be written as,

$$\begin{aligned} \dot{s}(t) = \;& \alpha_1 s(t-h) - \alpha_2 s(t) + (\beta - \gamma s(t-h) \\ & + \gamma s(t-\tau)) b(t-h) \end{aligned} \tag{20}$$

where α_i, β, γ, h and τ are positive constant parameters to identify. This type of model proved to be satisfactory in the context of separated flow such as a massively turbulent boundary layer or again a flow over an airfoil [26]. Identification of the model parameters is performed thanks to open-loop control experiments during which the flow response (reduced here to the drag signal) under various forcing is examined. The open-loop forcing experiments consist in successive cycles of actuation and relaxation phases for different values of the control parameters (here frequency F_A and duty-cycle DC). The range of the control parameters over which the flow response is explored must be sufficiently large such that the model can capture the essential changes in the flow due to actuation. In addition, robustness of the controller to changes in operational conditions can be significantly enhanced if the model identified can properly capture the resulting change in the flow response. The system response is thus first explored thanks to successive periodic forcings and the responses of the drag balance to the different actuation commands are then concatenated into a single time series. For conciseness, the reader is referred Feingesicht *et al.* [25] for full details of the identification procedure. In the present case, it leads to $\alpha_1 = 27.37$, $\alpha_2 = 32.70$, $\beta = 1.97$, $\gamma = 1.92$, $\tau = 0.18$ s and $h = 0.01$ s. The delay h represents the delay between a change in the input and a change in the output, usually called the input delay. However, the delay τ is a mathematical tool and cannot be directly related to a physical quantity, it is only obtained through identification and can take several different values that lead to a similar accuracy of the model.

The precision of the model has been evaluated by the following Fit index,

$$\text{Fit}(\%) = \left\{ 1 - \frac{\|s_{exp} - s_{sim}\|_{L_2}}{\|s_{exp} - \bar{s}_{exp}\|_{L_2}} \right\} \times 100\% \tag{21}$$

where s_{exp} is the output of the system obtained from the experiment, s_{sim} is the output of the identified bilinear model and $\bar{s}_{exp}$ denotes the mean value of s_{exp}. The obtained Fit index is equal to 59% for the present application. Note that only two time-delays are here retained in the modelling. As detailed in Feingesicht *et al.* [25], a better fit of the plant's response can be obtained if additional terms in Eq.

(20) are retained. However, this is done at the cost of an increase in the computation time needed to update the controller which is described in the next sections.

3.2.2. SMC *design for SISO flow control system*

Using Proposition 1 of Feingesicht *et al.* [25], we derive that the identified system is positive and its solutions are bounded as

$$0 \le s(t) < s_{\max} = \frac{\beta}{\alpha_2 - \alpha_1} \quad \text{for} \quad t > 0. \tag{22}$$

Let us introduce the following sliding variable

$$\begin{aligned} \sigma(t) = \; & s(t) - \sigma^* + \gamma \textstyle\int_{t-\tau+h}^{t} s(\mu)\mathrm{d}\mu \\ & + \textstyle\int_{t-h}^{t} (\alpha_1 s(\mu) + (\beta - \gamma s(\mu) \\ & + \gamma s(\mu - \tau + h))b(\mu))\mathrm{d}\mu \end{aligned} \tag{23}$$

where $\sigma^\star = s^\star(1 + \alpha_2 h + \gamma(\tau - h))$ and $s^\star \in \left(0, \frac{\beta}{\alpha_2 - \alpha_1}\right)$ is a predefined setpoint. The time derivative of σ is given by

$$\begin{aligned} \dot\sigma(t) \; & = (\alpha_1 - \alpha_2 + \gamma(1 - b(t)))s(t) + \\ & \gamma(b(t) - 1)s(t - \tau + h) + \beta b(t) \end{aligned} \tag{24}$$

For $b(t) = 1$ we obtain $\dot\sigma(t) = (\alpha_1 - \alpha_2)s(t) + \beta > 0$, but if $u(t) = 0$ one has $\dot\sigma(t) = (\alpha_1 - \alpha_2 + \gamma)s(t) - \gamma s(t - \tau + h) < 0$. Hence, one can be shown that there exists $t^* > 0$ such that $\sigma(t) = \sigma^*$ for all $t > t^*$. The system motion on the sliding surface is described by

$$s(t) + \alpha_2 \int_{t-h}^{t} s(\mu)d\mu + \gamma \int_{t-\tau}^{t-h} s(\mu)\mathrm{d}\mu - \sigma^* = 0 \tag{25}$$

The latter identity implies that $s(t) \to s^*$ as $t \to +\infty$. We refer reader to Feingesicht *et al.* [25] for more details about the proof of the asymptotic convergence.

3.2.3. Robustness of control system with respect to perturbations

Let us consider the perturbed model

$$\begin{aligned} \dot s(t) = \; & \alpha_1 s(t - h) - \alpha_2 s(t) + (\beta - \gamma s(t - h) \\ & + \gamma s(t - \tau))b(t - h) + p(t) \end{aligned} \tag{26}$$

where an admissible perturbation p is assumed to be bounded $|p(t)| \le \delta$ with some constant $\delta > 0$ and such that the perturbed system remains positive, i.e $s(t) \ge 0$ for any $t \ge 0$ and for any admissible p. In this case, any solution of the system is also bounded $0 \le s(t) \le (\beta + \delta)/(\alpha_2 - \alpha_1)$ for all $t \ge 0$.

Let the sliding surface σ be defined as before, but the set-point is selected as follows

$$s^* \in \left(\frac{\delta}{\alpha_2 - \alpha_1 - \gamma}, \frac{\beta - \delta}{\alpha_2 - \alpha_1}\right) \tag{27}$$

where $\delta > 0$ is a sufficiently small number such that the latter interval is nonempty. If $b(t) = 1$ we obtain $\dot\sigma(t) = (\alpha_1 - \alpha_2)s(t) + \beta + p(t) > 0$ for $s(t) \le (\beta - \delta)/(\alpha_2 - \alpha_1)$, but if $u(t) = 0$ one has $\dot\sigma(t) = (\alpha_1 - \alpha_2 + \gamma)s(t) - \gamma s(t - \tau + h) + p(t) < 0$ for $s(t) \ge \delta/(\alpha_2 - \alpha_1 - \gamma)$. For sufficiently small δ we can guarantee the sliding mode on the surface $\sigma = 0$ arises. The sliding motion equation in the perturbed case has the form

$$\begin{aligned} s(t) + \alpha_2 \textstyle\int_{t-h}^{t} s(\mu)d\mu + \quad & \gamma \textstyle\int_{t-\tau}^{t-h} s(\mu)d\mu - \sigma^* \\ & = \textstyle\int_{t-h}^{t} p(\mu)d\mu \end{aligned} \tag{28}$$

Using some elements of the theory of integral equations one can be shown that $s(t) \to s^* + O(h\delta)$ as $t \to +\infty$, where $O(\delta h)$ denotes a function of the order $h\delta$. This implies robustness of the control with respect to bounded perturbations and implies that the tracking error tends to zero as input delay h or perturbation magnitude δ tends to zero.

4. Results

Main features of the natural flow at $Re_h = 9 \times 10^4$ around a square-back Ahmed body are first presented in §4.1. Responses of the flow to open-loop forcing is then discussed in section §4.2 where two cases are considered: (1) a steady blowing case which is further taken into account as the "high-consumption" control reference case, and (2) a periodic forcing case for comparison with past studies. Finally, the first experimental results obtained for closed-loop using SMC are presented in §4.3.

4.1. Baseline flow

Key aspects of the unforced flow are initially analyzed. The static properties of the "natural"

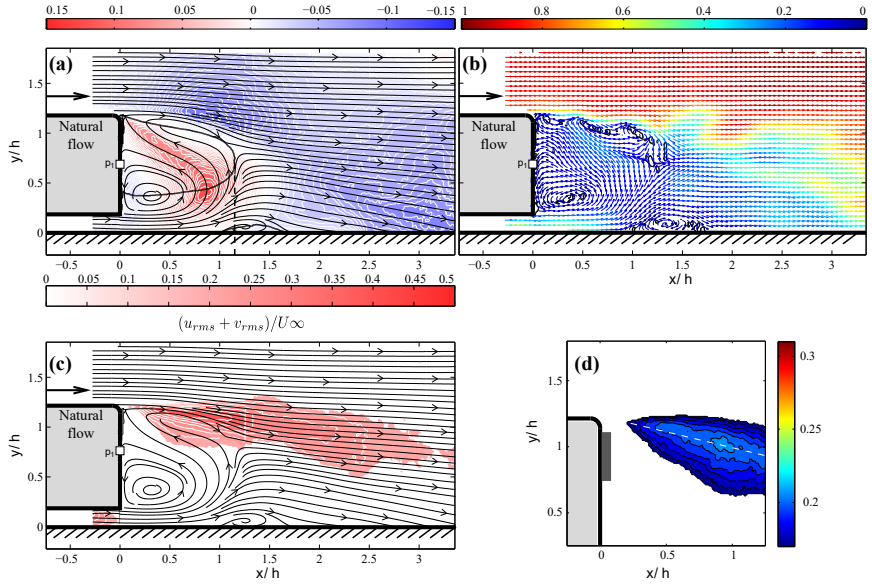

Figure 6: Natural flow characteristics in the symmetry plane (z = 0), (a) Time-averaged cross-stream velocity ($\bar{v}^+$) with the associate streamlines and the iso-line of the forward flow probability of 50%. The recirculating flow length L_r is also displayed by the vertical dashed line. (b) Instantaneous flow field #265 captured by the PIV. The velocity field is indicated by dimensionless norm colored arrows. The Γ_2 criterion is displayed by black iso-lines revealing the unforced shear-layer vortex street formation and the position of the classical main wake structures. (c) Contour map of the streamwise-transverse RMS-velocity ($u_{rms} + v_{rms}/U_\infty$) with associated streamlines.(d) closed view of the streamwise-transverse RMS-velocity.

flow are reviewed and the wake behaviour is first discussed. Bluff body wakes are sensitive to ground clearance (distance between the model under-surface and ground) and 3D spanwise effects. A slight variation on the ground clearance leads to a strong modifications of the wake structure, making them very sensitive to this parameter [32]. Figure 6(a) presents the time-averaged cross-stream velocity with associate streamlines and the iso-line for a forward flow probability of 50%. For the present case, a classical wall-normal asymmetry is obtained. However, the main flow from the ground clearance move toward the top edge of the body and then follows the upstream direction. This behaviour creates a large recirculation bubble located closer to the bottom edge and centred at x/h = 0.25 and y/h = 0.4; this configurations is known as an inverted asymmetric near wake. The presence of the Ahmed body support and pressure tube may also strongly perturbed the bottom edge flow. These perturbations generate a small recirculation bubble on the ground wall. A similar flow topology was found for studies with close ground distance [22]. Furthermore, an elongated recirculation area (black solid line) is clearly visible. The obtained recirculation length L_r = 1.15h (reported in Table 1) agrees well with previous studies [58, 36, 57]. The cross-stream velocity contour-plot shows the variability of the flow in the wall normal direction. A high normal motion (red region) is clearly observed, suggesting a strong positive wall normal velocity near the recirculation area.

Figure 6(b) shows a typical instantaneous vector velocity fields (coloured by the norm of the velocity vector) for the uncontrolled configuration. In order to highlight the unsteady flow structures, the vortex boundary identification method, introduced by Graftieaux *et al.* [31] is used herein. Two vortical structures appear, whereas the lower vortex is closer to the wall. Vortex creation at the top trailing edge are clearly seen, the presence of this coherent Kelvin-Helmholtz roll-ups in the vicinity of the upper edge, have a typical length scale of $\lambda_{KH} \approx 0.5h$. Due to convective KelvinHelmholtz-type instabilities, the created roll-up vortices evolve, amplified and further dissipate downstream. The amplification of these vortex creates an interaction between the upper and lower shear layers. Finally, the instantaneous snapshot clearly shows a strong flapping motion of the wake (associated to the shedding phenomena). The position and interaction of these vortex, caused by a perturbation, will enhance or diminish the drag.

The streamwise-transverse RMS-velocity ($(u_{rms} + v_{rms})/U_\infty$) is plotted in Figure 6 (c). A strong concentration of flow unsteadiness (red area) is presented along the shear layer, close to the top edge, corroborating the creation of unsteady flow structures in this region Figure 6(b). A small positive area is visible at the bottom edge, probably due to the perturbations created by the Ahmed body support and pressure tube. Also noteworthy is the influence of the RMS-velocity on the wake symmetry for which the creation of vortical eddies perturbs the wake and enlarge the bottom edge bubble. Similar results were obtained in different studies. Barros *et al.* [7] presented a strong streamwise-transverse velocity covariance $< \overline{u'v'} >$ close to the bottom edge and an asymmetric wake with a main bubble close to the top edge. While Grandemange *et al.* [32] obtained a symmetric stress ($< u'^* v'^* >$) and a symmetric wake. A closed view of the RMS-velocity is presented in Figure 6(d). The latter figure will be further used for comparison. The results presented in this section corroborate the strong influence of the bottom edge flow on the wake symmetry and the fact that small variation in the ground clearance may strongly influence wake behaviour.

4.2. Open-loop investigation

The response of both the baseline pressure and drag to various forcing parameters is here investigated. This paper follows the conventional terminology of Control Theory in order to split different control paradigms studied. Namely, we use the notion open-loop control if control input is independent of system output (measurements), as presented in Figure 8, and the closed-loop (or feedback) control, respectively, if the input is a

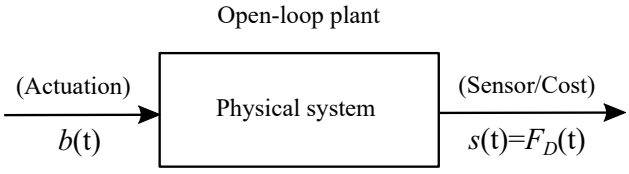

Figure 7: Sketch of open-loop control, where s denotes the sensor, herein the drag and b the actuation.

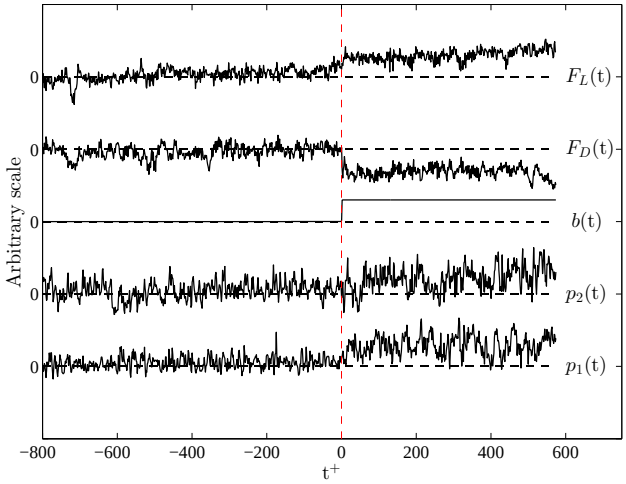

Figure 8: Time-histories response of the pressures and forces measurements due to a steady blowing step actuation (Re_h = 9×10^4, $C_{\mu 0}$ = 1.355%).

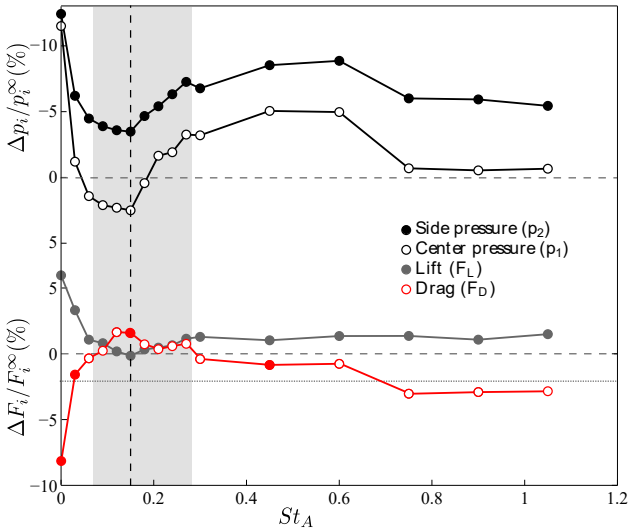

Figure 9: Normalized and averaged variations of the rear pressures p_i (p_1 and p_2), and forces F_i (lift F_L and drag F_D) compared to the natural case p_i^∞ and F_i^∞. These parameters are plotted as functions of the actuation frequency St_A at C_μ=0.00678 for Re_h = 9×10^4. The dash-line denotes the worst control case (St_o), corresponding to the wake shedding. Note that for the steady blowing (St_A = 0), the momentum coefficient is C_μ=0.01355 due to the duty cycle of the forcing cases. Filled red dots represent the four cases studied.

function of the output (see Figure 12). For a further understanding of the difference between open-loop and closed-loop control strategies used in the present article, a sketch of an Open-loop (OL) plant model is displayed in Figure 8, and defines the input/output parameters of the physical system used for flow control. With an open-loop control law it may be possible to achieve some desire specification without the use of measurement-based feedback control Brunton & Noack [13]. Two different forcing are here considered: continuous and periodical blowing.

First, the ability of steady blowing to modify the rear pressure, and consequently the drag, is investigated. The actuation cost for this specific case is $C_{\mu 0}$ = 1.355%. Figure 8 shows the time-history evolution of pressure and force measurements when a steady blowing actuation is applied. The vertical red dashed line indicates the instant when the actuation is turn on. The base pressure as well as the aerodynamic forces show significant variations when the actuation is activated. While the pressures at the back (p_2 and p_3) and the lift F_L increase, the drag F_D is found to decrease. Even though a focus in drag reduction is done in the present study, a significant increase in the lift is also of particular interest; few studies take into account this parameter [2] which is of great interest in transport industry. Future analysis and control of this force will be done for the configuration presented here.

The effect of periodic blowing on the rear pressure and drag is now described. The pulsating frequency f_A is varied in the range $[0-100]$ Hz, corresponding

to a Strouhal number St_A varying in $[0-1]$. Figure 9 shows the relative variations of pressures p_i and aerodynamic forces F_i compared to the natural case p_i^∞ and F_i^∞, against the dimensionless actuation frequency, St_A. An increase in the drag force is clearly seen for "low frequency" region $St_A \in [0, 0.15]$. A contrary behaviour is seen for the lift force (F_L) and the base pressure (p_i). The maximum drag value is obtained at the "worst" control case (St_o = 0.15). Following previous studies [22, 40], this Strouhal number corresponds to the wake shedding frequency (indicated by the vertical dashed line). This tendency is inverted for the "moderate frequency" region $St_A \in [0.15, 0.6]$, where the drag decreases. Again, an opposite tendency is obtained for F_D and p_i which well agrees with experimental and numerical investigations of the literature [52, 58]. The gray area in Figure 9 represents a positive drag difference, while the white area represents a negative drag difference. The optimal case, with a drag reduction up to −8%, is obtained for the steady blowing case (St_A = 0) but at the expense of a higher C_μ coefficient (1.355%) compared to that of the pulsating blowing cases (0.678%).

4.2.1. Wake modification

Effect of the open-loop forcing for different actuation frequencies on the near-wake flow is here discussed. Four different cases are considered and correspond to the red filled dots in Figure 9: (case I) steady-blowing case with St_A = 0, (case II) "low frequency" forcing case at $St_A = St_o/2$ leading to a negative drag difference, (case III) "low frequency" forcing case at $St_A = St_o$ implying a positive drag difference and (case IV) a "moderate frequency" forcing case at $St_A = 3St_o$ leading to a negative drag difference.

To understand how the base pressure and drag are affected by the forcing, modifications of the topology of the flow just at the rear of the body are first examined. Streamlines of the time-averaged velocity in the measurement plane for the four forcing cases are reported in Figures 10(a,d,g,j). The vertical dashed line shown in these figures correspond to the iso-line of the forward flow probability of 50%. The same information for the uncontrolled case is also reported for comparison as the red line. Finally, the colormap represents the level of the cross-stream velocity. An inverted asymmetric near-wake is observed for case I and II (Figure 10(a) and Figure 10(d) respectively). For these two cases, the height of the bubble is found to span almost half of the rear of the body while its length in the downstream direction is reduced compared to the two other forcing cases. For the steady blowing case I, the bubble is centred at the same location than that for the uncontrolled flow case (i.e. x/h = 0.25 and y/h = 0.4), while found closer to the bluff body wall for case II. For the other two arrangements, cases III and IV, a nearly symmetric flow with two large recirculation bubbles are observed (Figures 10(g) and 10(j) respectively) with the bottom one moving counter-clockwise and the upper one clockwise. When the actuation frequency is equal, or close, to that of the wake shedding ($St_A = St_o$) the bubbles are almost aligned in the x-direction with their focus at $x/h \approx 0.25$ as shown in Figure 10(g). In contrast, when the actuation frequency is higher than the wake shedding, the lower bubble moves closer to the wall, while the upper bubble is slightly shifted downstream as illustrated in Figure 10(j). Finally, one of the most important variables to determine the efficiency in drag reduction is the time-averaged cross-stream velocity. For all the forcing cases leading to a negative drag difference (cases I, II and IV) a region of positive mean cross-stream velocity is clearly seen, with a maximum cross-stream velocity closer to the wall than for the uncontrolled case. This behaviour defers for the positive drag case III ($St_A = St_o$) where the positive time-averaged cross-stream velocity nearly disappears.

The instantaneous velocity fields have been next examined in details. The full time sequences of these snapshots are available on-line; only the main features are discussed here. Figures 10(b),(e),(h) and (k) show instantaneous snapshots of some of the states for the actuated cases. For the steady blowing case, Figure 10(b), a direct opposition control of vortices in the near wake is applied. A continuous direct vortex perturbation in the top trailing edge shifts the convective structures closer to the body with a consequent reduction of the recirculation area. The upper and lower shear layer vortex interaction re-

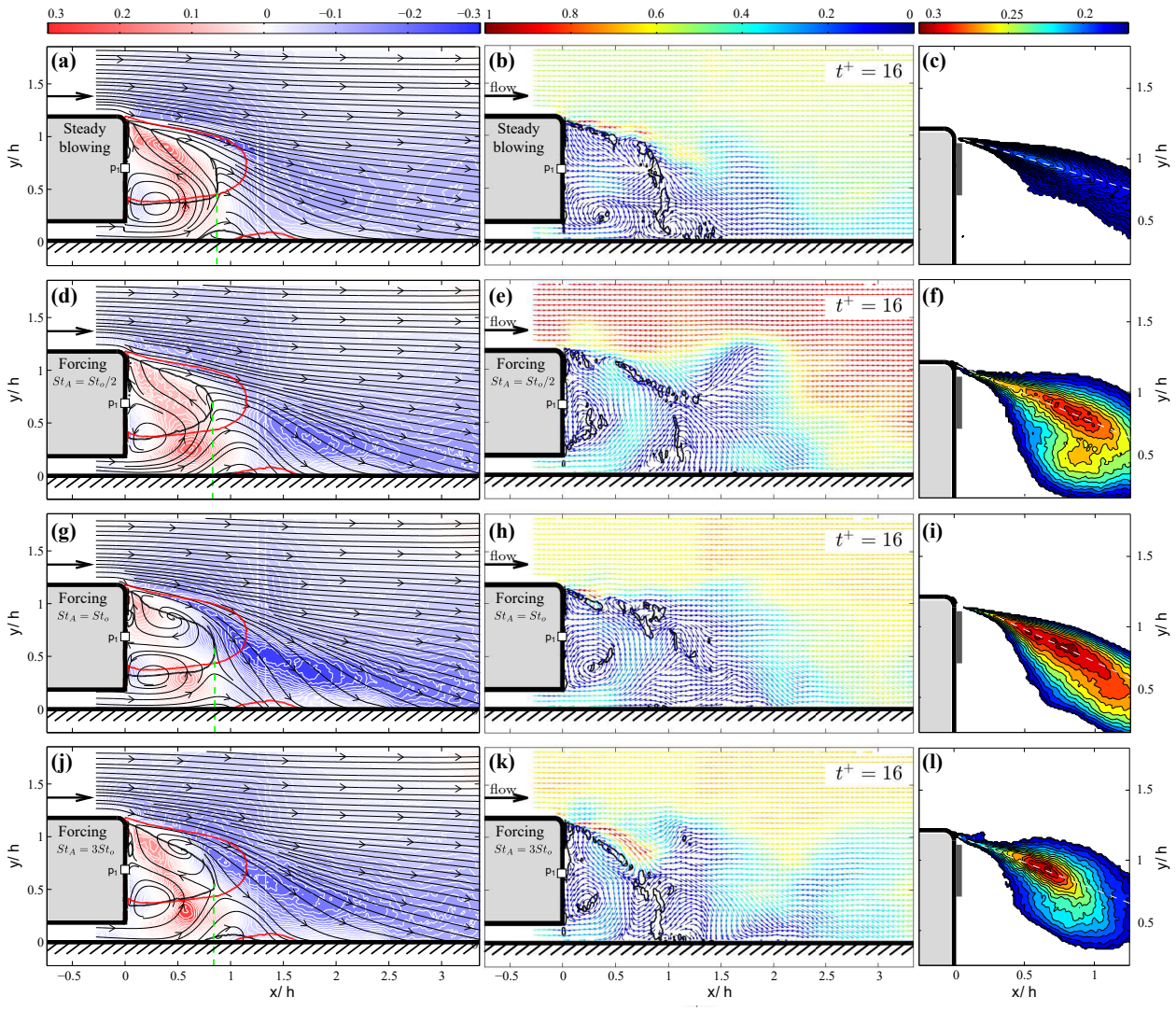

Figure 10: Forcing flow time-averaged cross-stream velocity ($\bar{v}^+$) with the associate streamlines, Instantaneous flow field #265 captured by the PIV and closed view of the streamwise-transverse RMS-velocity for several, (a,b,c) Case I: Steady blowing; (d,e,f) Case II: $St_A = St_o/2$; (g,h,i) Case III: $St_A = St_o$; (j,k,l) Case IV: $St_A = 3St_o$. The recirculating flow length L_r is displayed by the vertical dashed line. The iso-line of the forward flow probability of 50% is plotted in black for the controlled cases and in red for the natural flow reference. The velocity field is indicated by dimensionless norm coloured arrows. The Γ_2 criterion is displayed by black iso-lines revealing the unforced shear-layer vortex street formation and the position of the classical main wake structures. For a full visualization of the wake evolution please refer to the attached videos

approaches to the wall. The downward direct injection angle and the steady blowing combine together to deviate the trains of vortical structures, generated by the forcing, towards the rear face of the body as also observed by Barros *et al.* [7]

When periodic forcing is applied, the wake appears to be potentially modified through different processes depending on the forcing Strouhal number.
When an actuation with a Strouhal number below St_A = 0.15 (Case I) is applied, the wake is modified through energization of the shear-layer. As we approach a Strouhal number of 0.1, the sensitivity of shear-layers to low-frequency forcing are known to decrease, and the drag consequently increases due to decay in the locking effect at low actuation frequencies. Low frequency actuation will perform similarly to the continuous blowing case, which is consistent with the results of Figure 10(e) where a similar behaviour in the wake evolution as that observed for the continuous blowing case I is observed. These similarities corroborate the resemblance of the inverted asymmetric near for both continuous and low frequency forcing. For the periodic forcing, however, the large vortical structures are found to developed over the whole height of the body with eddied being present on a larger section of the cross-stream direction.
An interesting transition in the control process occurs for forcing Strouhal numbers St_A in $[0.15, 0.3]$ where the forcing is found to enhance the wake symmetry by affecting the vortex shedding mechanism. In this range of forcing Strouhal numbers, the drag force first increases up to reach a peak at forcing St_A equal to that of the wake shedding while decreasing once a symmetry in the wake is attained. Such wake symmetry is visible for Case III.

In addition, the proximity between the actuated and shedding frequencies leads to an expansion of the shear layer vortices close to the edge. The combination of a transitioning wake from asymmetric to symmetric- and a shear layer vortex expansion (unstable symmetry wake) could possibly lead to an increase in the cross-stream velocity and a decrease of the base pressure. It is noteworthy that the actuation is applied on the upper part only of the rear face of the body, which could possibly explain the instability of the symmetric wake. The results obtained here differ with some previous investigations [48, 7]. Nonetheless, similar results were obtained when the Ahmed body configuration and the actuation positioning are closer to the one presented here [22].
Finally, higher forcing frequencies $St_A > 0.3$ (case IV) are found beneficial with respect to the base pressure and drag. For such forcing case, a synchronization process between the upper and lower shear layers occurs such as observed in Figure 10(k), accompanied by small-scale vortices that maintain the wake symmetric wake.

Maps of the Rms-velocity are presented for the four forcing cases in Figures 10(c),(f),(i) & (k). Compare to the baseline flow (Figure 6(d)), the line of maximum velocity is found to move downward due to the negative actuation angle already discussed. While for the pulsed forcing cases are found to enhanced the maximum of velocity, a noticeable decrease is observed for the continuous blowing case. The later may be attributed to the narrow slit and large velocity of the actuation. For Case III (St_A = St_o) a thicker of intense region of Rms-velocity is obtained. The unsteady vortical structures, that are intensified by the periodic shedding frequency, strongly affect the near wake. The perturbed eddies are agglomerated close to the recirculation area intensifying the unsteady flow and further decreasing the cross-stream velocity. This analysis corroborates the flow structures presented in Figure 10(h) suggesting that an increase of the perturbed vortical structures (enhance of wake shedding) at the top trailing edge might have an impact in the drag rise. Cases II and IV present both a similar velocity pattern with rounded shape. The intensity of the area increases compared to the baseline flow, but not as strongly as for case II, ratifying the drag variation between the best and worst cases (case I and III respectively) suggesting that to decrease the drag, the forced structures must be moved near the wake while not strongly intensify.

To conclude this section, Barros *et al.* [7] described three different mechanisms for manipulating the

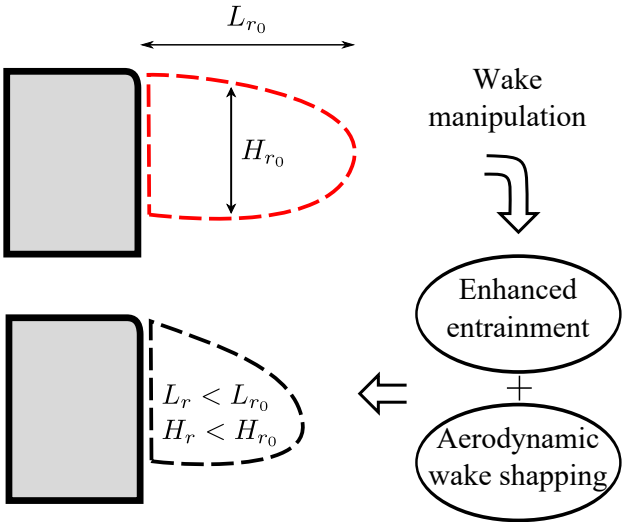

Figure 11: Global effect by wake manipulation: enhanced entrainment coupled to bubble shaping. Sketch is based on the results obtained by Barros *et al.* [7].

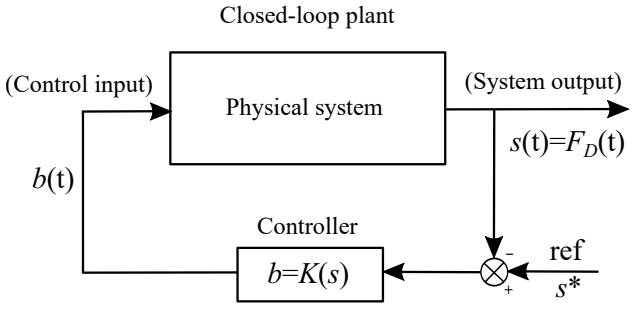

Figure 12: Sketch of closed-loop control. The loop performs the real-time closed-loop control. The plant feeds back the sensor output s to the controller K with regards to a tracking reference s^*. The controller computes the actuation command, b based on s and s^* and sends it back to the plant.

wake: (1) a reduction of entrainment and bubble elongation, (2) a reduction of entrainment coupled to bubble shaping for high-frequency forcing and finally, (3) a enhancement of entrainment decreasing the bubble length at low-frequency forcing. With regards to the results discussed previously, we here suggest a complementary mechanisms at play and illustrated in Figure 11. As initially mentioned, the actuation is directed downward by combining with Coanda effect. The vortical structures generated by the pulsed actuation are therefore convected downward while increasing the momentum entering into the wake. This results in a reduction of the thickness of the forced bubble as shown by Figure 10 and in an aerodynamic shaping of the rear flow. Nonetheless, other key parameters must be taken into account to properly understand the wake behaviour and further control it.

4.3. Sliding mode control

An overview of the closed-loop process implemented here is illustrated in Figure 12. A desired tracking reference point s^* is initially set by the user. The plant feeds back the sensor output ($s(t) = F_D(t)$) in real-time to the controller K. An actuation command $b(t)$ is computed based on $s(t)$ and s^* and it is finally fed back to the plant. The main goal is to track, reach and maintain the set-point, regardless of the flow perturbations presented upstream.

4.4. Experimental results of SMC *application*

The goal of this investigation is to reduce the drag to a desired value (set-point) and maintain it regardless incoming flow perturbations or again measurement noise and model inaccuracies. A maximum actuation switch frequency, f_{sw} is fixed at 100 Hz. To evaluate the cost of the control, the following instantaneous momentum coefficient is defined,

$$C^*_\mu(\mathrm{t}) = C_{\mu 0} \times DC^*(\mathrm{t}) = C_{\mu 0} \times \frac{1}{T_f} \int_{\mathrm{t}-T_f}^{\mathrm{t}} b(\tau)\mathrm{d}\tau \quad (29)$$

where $DC^*(t)$ defines the blowing fraction at time t averaged over a duration T_f. The Reynolds number is kept constant at $Re_h = 9 \times 10^4$ while the time window is $T_f = 60/f_{sw} = 0.3$ s. Based on the open-loop results discussed in the previous section, the set-point $s^* = -2.5\%$ is considered as the tracked value.

A resume of the results obtained with the SMC implemented is shown in Figures 13. Figures 13(a) shows the time response of the drag (top line) for

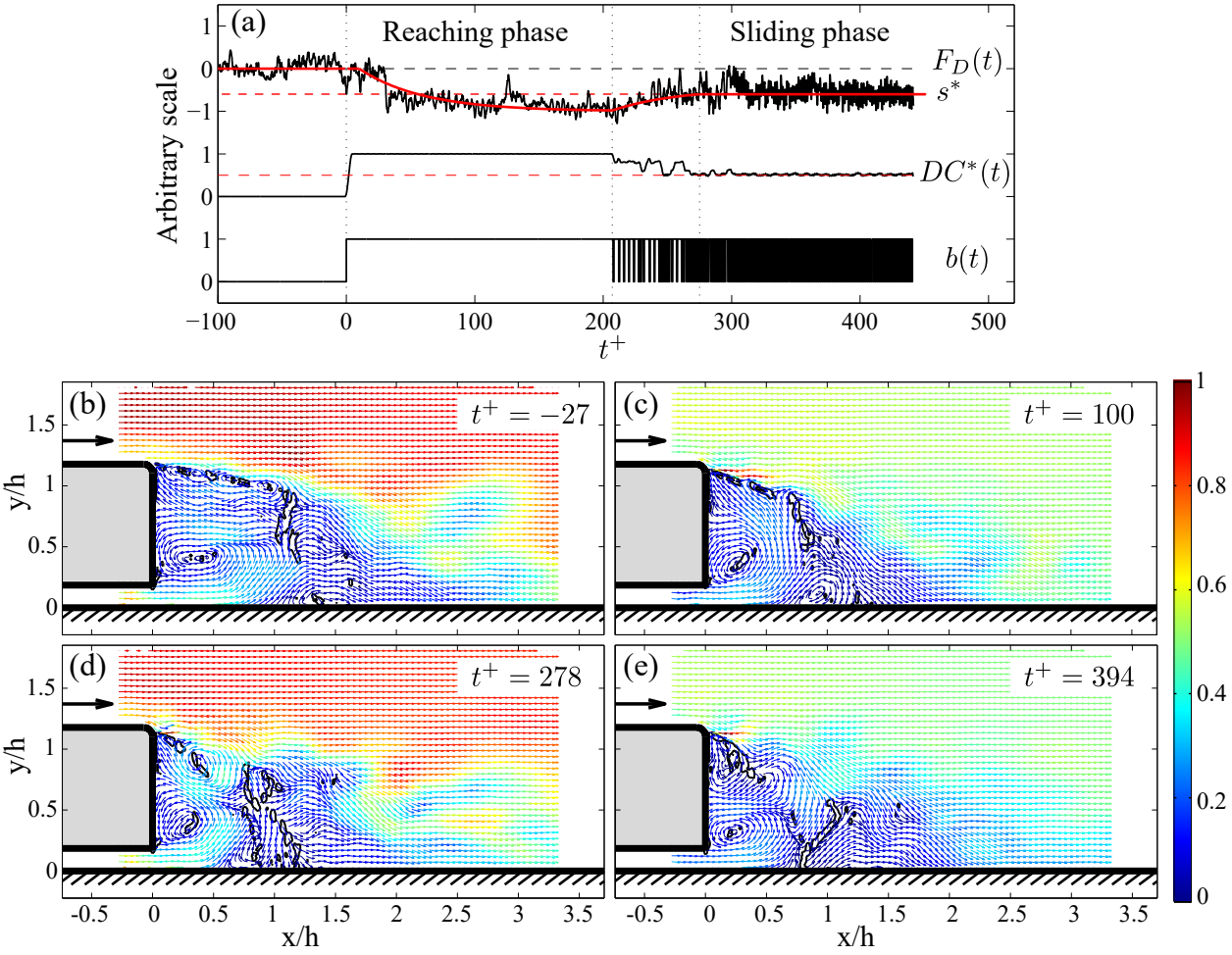

Figure 13: Sliding mode control set-point tracking results: upper plot shows the time history response of the drag force $F_D(t)$, control law $b(t)$ and the blowing fraction $DC^*(t)$. Instantaneous flow field captured by the PIV for several forced configurations time histories are plotted for: Unforced flow $t^+ = -27$, reaching phase $t^+ = 100$, transition $t^+ = 278$, sliding phase $t^+ = 394$

the forcing command $b(t)$ when the closed-loop controller is activated (bottom line). The calculated instantaneous duty cycle DC^* is also reported in this figure (middle line). Snapshots at four distinct instants of these time histories are reported in Figures 13(b-e). Three distinct control phases are noticeable in Figures 13(a). When the actuation is activated ($t^+ = 0$), the controller enters a phase known at "reaching phase" whose objective is to approach rapidly the targeted set-point and during which the drag force is found to decrease rapidly. In the present case, this phase corresponds to a steady blowing forcing as seen in Figures 13(a) where the DC^* is found equal to unity. The duration of this phase can be chosen by the user and was, in the present work, stopped at $t^+ = 200$. A transition phase ($200 < t^+ < 280$) is then observed during which the controller seeks the adequate ON-OFF combination to rapidly reach the targeted set-point. Finally, the last phase ($t^+ > 280$) corresponds to the so-called "sliding phase" where the controller attempts to maintain the drag at the tracked value s^* despite any disturbances on the plant.

The different stages reached by the near-wake flow can be examined thanks to the instantaneous snapshots of Figures 13(b-e). During the unactuated phase ($t^+ < 100$), Figures 13(b), a train of vortices at the top trailing edge is clearly visible where the shear layer roll-ups evolve and convect downstream. The shear layers interaction with the near wake creates an inverted asymmetric topology as already discussed in §4.1. During the reaching phase, Figure 13(c), since the actuation corresponds to a steady blowing forcing, the near-wake flow resembles that described for the open-loop case I with the presence of an asymmetric wake behaviour, a shift of the convective structures closer to the recirculation and a development of large vortical structures evolving near ground. During the transition phase, Figure 13(d), a transition in the near-wake shape is noticeable. The flow is evolving from an asymmetric configuration (energization of the shear layer) to a symmetric one (strengthening of the wake symmetry by forcing the vortex shedding), as also obtained for the open-loop case III. This transition of the sliding mode mechanisms - and further wake variation- triggers a periodic forcing modification that will increase the drag force, as seen in Figure 13(a). Finally, once the actuation is in the sliding phase, a synchronization of both shear layers is clearly observed (Figures 13(e)) similar to that identified in open-loop case IV. The implemented controller is therefore found satisfactory in terms of set-point tracking with, in particular, a negligible steady-state error.

5. Conclusion and perspective

Open- and closed-loop strategies are examined targeting the drag reduction of a turbulent flow around a square-back Ahmed body. Complementary velocity fields acquired from particle image velocimetry are presented. The impact of steady blowing and periodic forcing as open-loop control strategies on the wake are first investigated. The actuation is performed with pulsed jets at the top trailing edge combined with an angle effect, similar to a Coanda effect. The addition of the Coanda effect to the actuator system reinforces the flow deviation close to the model. The flow is monitored in time with pressure, lift and drag sensors. The optimal case control law is steady blowing ($St_A = 0$), with a drag reduction up to -8%. An increase in both the drag force is clearly seen for the "low frequency" regime $St_A \in [0, 0.15]$. A decrease in the force is seen after $St_A = 0.15$. A shortening of both the recirculation length and height is cause by a direct perturbation (due to angle effect) of the pulsed jet vortical eddies. For a "low frequency" regime, the near-wake instabilities are strongly dependant on the Strouhal number variation. A transition in the flow wake will decrease the cross-stream velocity and increase the drag force. On the contrary, for "moderate frequency" regimes ($St_A > 0.15$) the actuation generates small vortices close to the edge, induces roll-up evolution, which keeps the wake symmetry and reduces the drag. These results might improve our understanding of how bluff body drag varies with low- and high- wake forcing, which is crucial to find novel control strategies and implementations [13]. For a closed-loop approach, we present a novel, robust closed-loop control to reduce and maintain the drag. To the authors knowledge, the first experimental result using sliding mode control (SMC)

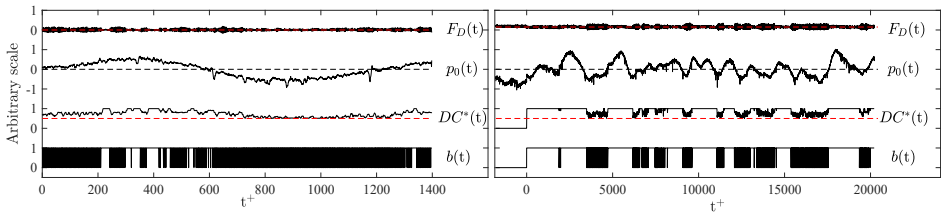

Figure 14: Disturbance rejection results. Figures show the time history response of the control law $b(t)$ and the blowing fraction DC^*(t) for: left) a sinusoidal up-stream perturbation p_0; right) randomly generated up-stream perturbation.

is here presented in the context of flow control. We are interested in minimizing the drag to a set-value s^* and stabilizing it regardless external conditions.

The control approach is based on an initial black-box model identification presented by Feingesicht *et al.* [25]. The set of data obtained from open-loop control were used for the model design. In principle, the control approach can be seen as a compilation of open-loop control tests. However, the actuation frequency has to be selected carefully in real-time depending on the external parameters up- and down-stream of the flow. Otherwise, actuation energy is wasted. The robustness and easy implementation in an experimental setup make this approach convenient for industrial applications.

To corroborate robustness and efficiency of this control approach, a second experiment was conducted to show disturbance rejection of the controller. Figures 14 shows two different up-stream flow perturbations $p_0(t)$ with corresponding drag force F_D and generated control law $b(t)$. Its is possible to see how the control law is adapted to maintain the drag force at the desired s^* value. The controller, unaware of the up-stream disturbances, reacts immediately and drives the system to the set-point. The control limitation will come with the actuator capacity. If the drag strongly increases, the control command will apply continuous blowing. On the contrary, if the drag is reduced, the control will stop and wait for an increase of F_D up to the desired value. The set-point determination and actuators' limitation are of great importance to arrive to a successful and robust control approach. The present results suggest that the implemented controller has a satisfactory performance in disturbance rejection. In real world applications, flow control has to subsist with varying oncoming velocities, high turbulence levels and other perturbations. Hence, the benefits of sliding mode control can be fully exploited. In future work, the authors will pursue a SIMO model to improve wake stabilization. Also, the control performance will be graded by energy consumption. Finally, in order to prove the feasibility of such approach in a full-scale environment, a project where a real car model will be fully equipped is currently ongoing.

Acknowledgments

This work was carried out within the framework of the CNRS Research Federation on Ground Transports and Mobility, in articulation with the Elsat2020 project supported by the European Community, the French Ministry of Higher Education and Research, the Hauts de France Regional Council. The authors gratefully acknowledge the support of these institutions.The authors declare that they have no conflict of interest.

[1] Ahmed, S. R., Ramm, G. & Faltin, G. 1984 Some salient features of the time averaged ground vehicle wake. *Society of Automotive Engineers, SAE Inc* **840300**.

[2] Aider, J. -L, Beaudoin, J. -F & Wesfreid, J.E. 2009 Drag and lift reduction of a 3D bluff-body using active vortex generators. *Exp. Fluids* **49**: 771-89.

[3] Amitay, M., Smith, D.R., Kibens, V., Parekh, D. & Glezer, A. 2001 Aerodynamic

Flow Control over an Unconventional Airfoil Using Synthetic Jet Actuators *AIAA journal* **39**(3), 361-370.

[4] Arduino Co. 2008 All Rights Reserved. *www.arduino.cc*.

[5] Aubrun, S., McNally, J., Alvi, F. & Kourta, A. 2011 Separation flow control on a generic ground vehicle using steady microjet arrays. *Exp. Fluids* **51**(5): 1177-11878.

[6] Baker, C. 2010*a* The flow around high-speed trains *J. Wind. Eng. Ind. Aerodyn.* **98**: 277-98.

[7] Barros, D., Borée, J., Noack, B.R., Spohn, A. & Ruiz, T. 2016*b* Bluff body drag manipulation using pulsed jets and Coanda effect. *J. Fluid Mech.* **805**: 422-459.

[8] Barros, D., Borée, J., O., Cadot., A., Spohn & Noack, B. R. 2017 Forcing symmetry exchanges and flow reversals in turbulent wakes. *J. Fluid Mech.* **829**.

[9] Becker, R., King, R., Petz, R. & Nitsche, W. 2007 Adaptive Closed-Loop Separation Control on a High-Lift Configuration Using Extremum Seeking.*AIAA journal* **45**(6), 15382-1392.

[10] Becker, R., Garwon, M., Gutknecht, C., Barwolff, G. & King, R. 2015 Robust control of separated shear flows in simulation and experiment. *J. Process Control* **15**(6): 691-700.

[11] Brackston, R., Wynn, A. & Morrison, J. F. 2016 Extremum seeking to control the amplitude and frequency of a pulsed jet for bluff body drag reduction. *Exp. Fluids* **57**(10):159.

[12] Bradley, R. 2015 Technology roadmap for the 21st century truck program. *Tech. Rep.* 21CT-001, US Dep. Energy, Washington, DC.

[13] Brunton, S. L. & Noack, B. R. 2015 Closed-loop turbulence control: Progress and challenges. *Appl. Mech. Rev.* **67**(5), 050801:01-48.

[14] Brunn, A., Wassen, E., Sperber, D., Nitsche, W. & Thiele, F. 2007 Active Drag Control for a Generic Car Model. *Active flow control NNFM* **95**, pp. 247-259. Springer - Heidelberg.

[15] Cattafesta, L. & Shelpak, M. 2011 Actuators for active flow control. *Ann. Rev. Fluid Mech.* **43**: 247-272.

[16] Deem, E., Cattafesta, L., Zhang, H., Rowley, C., Hemati, M., Cadieux, F., & Mittal, R. 2017 Identifying Dynamic Modes of Separated Flow Subject to ZNMF-based Control from Surface Pressure Measurements. *47th AIAA Fluid Dynamics Conference*, pp. 1-19. Denver, Colorado.

[17] Choi, H., Lee, J. & Park, H. 2014 Aerodynamics of heavy vehicles. *Ann. Rev. Fluid Mech.* **46**: 441-468.

[18] Chovet, C., Keirsbulck, L., Noack, B. R., Lippert, M. & Foucaut, J.-M. 2017 Machine learning control for experimental shear flows targeting the reduction of a recirculation bubble. *20th World Congress IFAC*, pp. 1-4, Toulouse, France.

[19] Detemple-Laake, E., & Eckelmann, H. 1989 Phenomenology of Karman vortex streets in oscillatory flow. *Exp. Fluids* **7**: 217-227.

[20] Duriez, T., Brunton, S. & Noack, B. R. 2016 *Machine Learning Control — Taming Nonlinear Dynamics and Turbulence. Fluid Mechanics and Its Applications* **116**. Springer-Verlag.

[21] Englar, R. J. 2004 Pneumatic heavy vehicle aerodynamic drag reduction, safety enhancement, and performance improvement. *The Aerodynamics of Heavy Vehicles: Trucks, Buses, and Trains*, pp. 277-302, Springer.

[22] Eulalie, Y. 2007 Aerodynamic analysis and drag reduction around an Ahmed bluff body. PhD. *thesis*, Bordeaux Univ.

[23] Evstafyeva, O., Morgans, A. S. & Dalla Longa, L. 2016*b* Simulation and feedback control of the Ahmed body flow exhibiting symmetry breaking behaviour *J. Fluid Mech.* **817**: R2.

[24] Feingesicht M., Raibaudo, C., Polyakov A., Kerhervé F. & Richard J. -P. 2016 A bilinear input-output model with state-dependent delay for separated flow control *European Control Conference* Aalborg, Denmark.

[25] Feingesicht M., Polyakov A., Kerhervé F. & Richard J. -P. 2017 SISO model-based control of separated flows: Sliding mode and optimal control approaches. *Int. J. Robust and Nonlinear Control* **27**(18), 5008-5027, DOI:10.1002/rnc.3843.

[26] Feingesicht, M. 2017 Contrôle non linéaire actif découlements turbulents décollés : Théorie et expérimentations. PhD. *thesis*, Inria/CRIStAL, France.

[27] Gautier, N. & Aider, J. -L 2013 Control of the flow behind a backwards facing step with visual feedback. *Proc. R. Soc. Lond* A **469**,2160.

[28] Gautier, N. & Aider, J. -L 2014*a* Frequency lock closed-loop control of a separated flow using visual feedback. *J. Fluid Mech.* **759**, 181-196.

[29] Gautier, N., Aider, J. -L., Duriez, T., Noack, B. R., Segond, M. & Abel, M. W. 2015 Closed-loop separation control using machine learning. *J. Fluid Mech.* **770**, 424-441.

[30] Glezer, A., Amitay, M. & Honohan, A. M. 2005 Aspects of low-and high-frequency actuation for aerodynamic flow control. *AIAA journal* **43**(7), 1501-1511.

[31] Graftieaux L., Michard M. & Grosjean N. 2001 Combining Piv, Pod and vortex identification algorithms for the study of unsteady turbulent swirling flows. *Measurement science and technology* **12**, 1422-1429.

[32] Grandemange, M., Gohlke, M. & Cadot, O. 2016*b* Turbulent wake past a three-dimensional blunt body. Part 1. *J. Fluid Mech.* **722**: 51-84.

[33] GHan, T., Hammond, D. C. & Sagi, C. J. 1992 Optimization of bluff body for minimum drag in ground proximity. *AIAA Journal* **30**(4), 882-889.

[34] Hucho, W. -H., e.d. 1998 *Aerodynamics of road vehicles.* Society of Automotive Engineers.

[35] Huerre, P. & Monketwitz, P. A. 1990 Local and global instabilities in spatially developing flows. *Ann. Rev. Fluid Mech.* **22**: 473-537.

[36] Lahaye, A., Leroy, A. & Kourta, A. 2014 Aerodynamic characterisation of a square back bluff body flow. *Int. J. Aerod.***4**(1-2), 43-60.

[37] Li, R., Noack, B. R., Cordier, L., Borée, J. & Harambat, F. 2017*a* Drag reduction of a car model by linear genetic programming control. *Exp. Fluids***58**(103), 1-20.

[38] Krajnović, S. & Davidson, L. 2005*a* Flow around a simplified car, Part 1: Large Eddy Simulation. *J. Fluids Engeg.* **127(5)**, 907-918.

[39] Krajnović, S. & Davidson, L. 2005*b* Flow around a simplified car, Part 2: Understanding the flow. *J. Fluids Engeg.* **127(5)**, 919-928.

[40] Krajnović, S. & Fernandes, J. 2010 Numerical Simulation of the flow around a simplified vehicle model with active flow control. *Int. J. of Heat and Fluid Flow* **32(1)**, 192-200.

[41] Krentel, D., Muminovic, R., Brunn, A., Nitsche, W. & King, R. 2010 Application of active flow control on generic 3D car models.. *Active flow control II*, pp.223-239. Springer.

[42] McCallen, R. C., Salari, K., Ortega, J. M., DeChant, L. J., Hassan, B., Roy, C. J., Pointer, W. D., Browand, F., Hammache, M., Hsu, T.-Y., Leonard, A., Rubel, M., Chatelain, P., Englar, R.,

Ross, J., Satran, D., Heineck, J. T., Walker, S., Yaste, D. & Storms, B. 2004 DOE's Effort to Reduce Truck Aerodynamic Drag - Joint Experiments and Computations Lead to Smart Design. *AIAA Paper*, 2014-2249.

[43] Oxlade, A. R, Morrison, J. F., Qubain, A. & Rigas, G. 2015 High-frequency forcing of a turbulent axisymmetric wake. *J. Fluid Mech.* **770**, 305-318.

[44] Park, H., Lee, D., Jeon,W.-P., Hahn, S., Kim, J., Kim, J., Choi, J. & Choi, H. 2006 Drag reduction in flow over a two-dimensional bluff body with a blunt trailing edge using a new passive device. *J. Fluid Mech.* **563**, 389-414.

[45] Park, H., Cho, J.-H., Lee, J., Lee, D. -H. & Kim, K. -H 2013 Aerodynamic drag reduction of Ahmed model using synthetic jet array. *Tech. Rep.* SAE Technical Paper

[46] Parezanović, V., Cordier, L., Spohn, A., Duriez, T., Noack, B. R., Bonnet, J.-P., Segond, M., Abel, M. & Brunton, S. L. 2016 Frequency selection by feedback control in a turbulent shear flow. *J. Fluid Mech.* **797**, 247-283.

[47] Parezanović, V., Laurentie, J. C., Fourment, C., Delville, J., Bonnet, J. P., Spohn, A., Duriez, T., Cordier, L., Noack, B. R.& Abel, M. 2015 Mixing layer manipulation experiment: From open-loop forcing to closed-loop machine learning control. *Flow. Turb. Comb.* **94**(1), 155-173.

[48] Pastoor, M., Henning, L., Noack, B. R., King, R. & Tadmor, G. 2008 Feedback shear layer control for bluff body drag reduction. *J. Fluid Mech.* **608**, 161-196.

[49] Polyakov A. 2012 Minimization of disturbances effects in time delay predictor-based sliding mode control systems. *Journal of the Franklin Institute* **39**(4): 1380-1396.

[50] Raghunathan, R. S., Kim, H. D. & Setoguchi, T. 2002 Aerodynamics of high-speed railway train. *Prog. Aerosp. Sci.* **38**: 469-514.

[51] Richard J.P., Gouaisbaut F. & Perruquetti W. 2001 Sliding mode control in the presence of delay. *Kybernetika* **37**(3): 277-294.

[52] Rouméas, M., Gilliéron, P. & Kourta, A. 2009 Drag reduction by flow separation control on a car after body. *Int. J. Num. Meth. Fluids* **60**(11): 1222-1240.

[53] Schmidt, H.J., Woszidlo, R., Nayeri, C. N. & Paschereit, C. O. 2015 Drag reduction on a rectangular bluff body with base flaps and fluidic oscillators. *Exp. Fluids* **56**(7): 1-16.

[54] Sontag, E.D. 2005 Input to state stability: Basic concepts and results. *Springer Lecture Notes in Mathematics* **CIME Course**, Cetraro.

[55] Tanner, M. 1972 A method of reducing the base drag of wings with blunt trailing edges. *Aeronaut. Q***23**, 15-23.

[56] Utkin, V. 1991 Sliding Modes in Control Optimization. *CCES Springer-Verlag*, Berlin.

[57] Volpe, R., Devinant, P. & Kourta, A. 2015 Experimental characterization of the unsteady natural wake of the full-scale square back Ahmed body: flow bi-stability and spectral analysis. *Exp. Fluids* **56**(5): 1-22.

[58] Wassen, E., Eichinger, S. & Thiele, F. 2010 Simulation of active drag reduction for a square-back vehicle. *Active flow control II*, pp. 241-255. Springer

[59] Wiltse, J. M. & Glezer, A. 1998 Direct exctitation of small-scale motions in free shears flows. *Phys. Fluids* **10**: 2026-2036.

[60] Yi, W. 2007 Drag reduction of a three-dimensional car model using passive control device. PhD. *thesis*, Seoul Natl. Univ.

[61] Zhang, M., Cheng, L. & Zhou, Y. 2004 Closed-loop-controlled vortex shedding and vibration of a flexibly supported square cylinder under different schemes. *Phys. Fluids* **16**(5): 1439-1448.